RESEARCH ARTICLE | MAY 23 2025

Decoupling light redistribution from absorption via waveguide-integrated bilayer metagratings

Xin Zhou ; Zepeng Zhuang; Xintao He ; Jianwen Dong

J. Appl. Phys. 137, 203104 (2025)
https://doi.org/10.1063/5.0267304

Journal of Applied Physics ARTICLE pubs.aip.org/aip/jap

Decoupling light redistribution from absorption via waveguide-integrated bilayer metagratings

Cite as: J. Appl. Phys. **137**, 203104 (2025); doi: 10.1063/5.0267304
Submitted: 23 February 2025 · Accepted: 7 May 2025 ·
Published Online: 23 May 2025

View Online Export Citation CrossMark

Xin Zhou,[1] Zepeng Zhuang,[1,2] Xintao He,[1] and Jianwen Dong[1,a)]

AFFILIATIONS

[1]State Key Laboratory of Optoelectronic Materials and Technologies and School of Physics, Sun Yat-sen University, Guangzhou 510275, China
[2]State Key Laboratory of Surface Physics, Key Laboratory of Micro and Nano Photonic Structures (Ministry of Education), Shanghai Key Laboratory of Metasurfaces for Light Manipulation and Department of Physics, Fudan University, Shanghai 200438, China

[a)]**Author to whom correspondence should be addressed:** dongjwen@mail.sysu.edu.cn

ABSTRACT

Integrated optical systems, encompassing microwave photonics, optical communication receivers, and optical sensing, require photodetectors with high saturation power and responsivity. Achieving uniform and efficient light absorption is essential for realizing these properties. However, traditional waveguide-coupled photodetectors struggle with a trade-off between absorption efficiency and uniformity due to exponential intensity decay in the waveguide direction. In this work, we propose waveguide-integrated bilayer metagratings that decouple light redistribution from absorption, achieving uniform and efficient absorption simultaneously. By elucidating the fundamental physics governing resonant mode coupling between the upper silicon metagrating (Si MG) and waveguide, we demonstrate that the Si MG couples out the waveguide mode and redistributes its intensity uniformly with 84% coupling efficiency. The lower germanium metagrating (Ge MG), serving as the absorber, achieves 90% absorption efficiency via guided-mode resonance. Compared with traditional evanescent coupling, this design enhances light intensity uniformity in the germanium absorption region while maintaining >70% overall efficiency. This approach holds promise for resolving the uniformity-efficiency trade-off in waveguide-coupled photodetectors, while extending beyond germanium systems to provide a strategy for III–V/Si hybrid integration in applications ranging from LIDAR receivers to quantum photonic processors.

I. INTRODUCTION

Silicon photonics has emerged as a promising platform for photonic integrated circuits owing to its compatibility with conventional complementary metal–oxide–semiconductor (CMOS) manufacturing processes.[1–5] Integrated optical systems, including microwave photonics, optical communication receivers, and optical sensing, necessitate photodetection devices with high power and high responsivity.[6–12] These performance metrics are fundamentally governed by absorption uniformity and efficiency. In waveguide-coupled photodetectors, the incident light propagates within the waveguide and is coupled into the absorbing material, such as Ge or III–V materials, via evanescent waves. This evanescent coupling approach creates a fundamental physical trade-off: while longer waveguide lengths can improve total absorption efficiency,[13–15] the non-uniform absorption profile caused by exponential optical intensity attenuation along the waveguide length direction leads to severe carrier screening under high optical power.[16,17] Existing solutions encompass waveguide side-coupling[18–20] and simultaneous multi-port coupling.[21–23] However, these methods merely optimize the spatial uniformity of optical intensity to the extent possible without fundamentally resolving this trade-off, while introducing complex waveguide networks incompatible with dense integration.

As fundamental components in optical communication and sensing systems, metagratings have attracted considerable research interest in recent years.[24–26] Specifically, metagratings have demonstrated unique advantages in on-chip beam coupling and shaping,[27] as well as in enhancing light absorption.[28] In terms of on-chip beam coupling and shaping, metagratings have exhibited significant capabilities in coupling guided modes into free space by converting waveguide modes into radiation modes.[29–32] Typically, the radiation modes are designed to efficiently generate Gaussian intensity distributions, which are useful for fiber-to-chip coupling[33–37] and gas spectroscopy.[29,30] Furthermore, radiating light beams with a uniform intensity distribution in free space show potential for enhancing the resolution of fluorescence nanoscopy.[38,39] On the other hand, the surface plasmon resonance[40–43] or guided-mode resonance (GMR) effects[44–46] of metagratings have been demonstrated to enhance light absorption. However, due to limited degrees of freedom in single-layer metagrating designs, it is challenging to simultaneously achieve on-chip mode field distribution control and light absorption efficiency regulation. Recently, bilayer metagratings have been shown to provide greater degrees of freedom for designing efficient light coupling, shaping, and topological GMR in comparison with single-layer gratings,[47–52] suggesting the possibility of overcoming this constraint. However, their potential for solving the uniformity-efficiency paradox in photodetection remains unexplored.

In this work, we propose waveguide-integrated bilayer metagratings that decouple light redistribution from absorption processes to achieve uniform and efficient light absorption, using a silicon-based germanium material system as an example. The core of this work lies in the separation of light manipulation processes: the silicon metagrating (Si MG) acts as a mode converter to extract and homogenize waveguide-confined light, while the Ge MG operates as a resonant absorber independent of propagation-length constraints. We elucidate the fundamental physics governing resonant mode coupling between the Si MG and the waveguide. By exploiting the strong coupling between the grating and waveguide modes, the Si MG efficiently couples the incident waveguide-propagating light into free space with 84% coupling efficiency and redistributes the optical intensity uniformly across the $15 \times 3\,\mu\text{m}^2$ area. The Ge MG enhances light absorption efficiency via the GMR effect, thereby achieving an absorption efficiency as high as 90%, which is five times higher than that of an optical thin film of the same thickness. Compared with conventional waveguide evanescent coupling methods, the waveguide-integrated bilayer metagratings approach enables a more uniform distribution of the optical field intensity within the Ge absorption region. The total light absorption efficiency can still exceed 70% by adjusting the thickness of the spacer layer between the two metagratings. We also investigate the parameter sensitivity and the impact of temperature variations on the total absorption efficiency. This work holds great promise for enhancing silicon-based germanium photodetector performance, particularly its saturation power and responsivity. Prior studies have already achieved fabrication processes including bilayer integrated nanophotonic structures[52] and Ge etching[12] on silicon-on-insulator substrates, which confirm the feasibility of our proposed waveguide-integrated bilayer metagratings. The principles can extend beyond Ge systems, offering a framework for III–V/Si hybrid integration in applications from LIDAR receivers to quantum photonic processors.

II. RESULTS AND DISCUSSION

Our structural design is based on a Silicon-On-Insulator (SOI) substrate. Figure 1 illustrates the schematic diagram of the proposed waveguide-integrated bilayer metagratings. First, the bidirectional

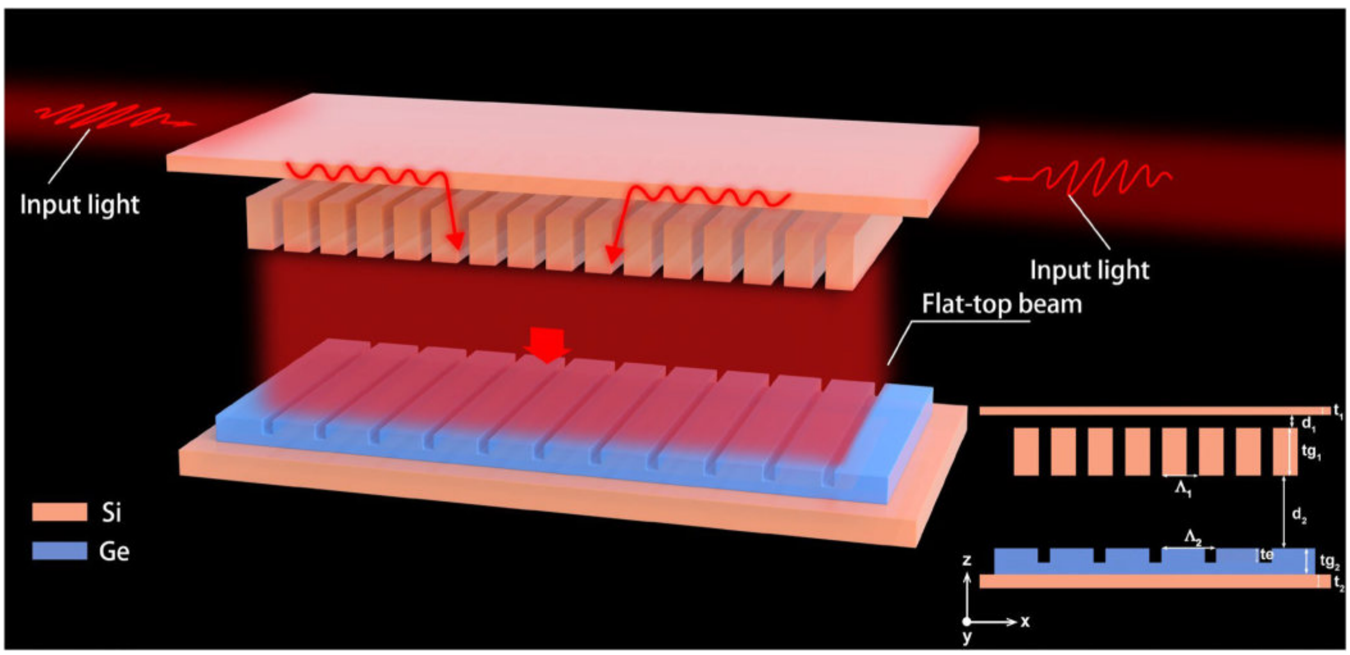

FIG. 1. Schematic illustration of the three-dimensional structure of waveguide-integrated bilayer metagratings, with the inset in the lower right corner showing a two-dimensional cross-sectional view of the xz-plane.

propagating transverse-electric (TE, electric field along y-direction) polarized light, within the topmost Si waveguide, is efficiently coupled into the free space between Si MG and Ge MG. Flat-top beam shape is realized at the same time, leading to the uniform intensity distribution in the Ge MG. Second, the downward flat-top beam is then absorbed by the Ge MG, enhanced by the designed guided-mode resonance in this region. Beneath the Ge MG, there lies a 220 nm-thick SOI slab waveguide. The side view of the total structure is presented in the lower right corner of Fig. 1. Note that our design in this work focuses on TE polarization. For a TM-polarized device, one can insert a TM-to-TE mode converter at the front of the proposed metagrating device.

A. Analysis of physical mechanisms governing mode coupling between Si MG and waveguide

For the upper Si MG, high coupling efficiency and flat-top out-coupling beam shape is critical. For an ideal case, where bidirectional propagating waveguide modes are perfectly converted into an infinite flat-top beam without any loss, its reciprocal process is also satisfied. Actually, this process exactly corresponds to the transformation of a plane wave into two bidirectional propagating waveguide modes. As a result, instead of considering the complex process in the forward case, we look into the reciprocal case and design the upper Si MG.

When a plane wave is coupled into the waveguide through the Si MG, the wavevector matching condition asks for the following equation:

$$n_0 \sin\theta_i + m\frac{\lambda}{\Lambda_1} = n_{\text{eff}}. \tag{1}$$

Here, n_{eff} is the effective refractive index of the waveguide mode, θ_i is the incident angle, m is the diffraction order of the grating, n_0 is the refractive index above the incident plane, and Λ_1 is the grating period. For normal incidence, $\theta_i = 0$ and to prevent the incident light from leaking into higher diffraction orders, m is typically set to 1. In this case, only the zeroth and first diffraction orders survive. Noting that only the first diffraction order is wanted, one has to suppress the zeroth order for high coupling efficiency. For this purpose, resonant modes in Si MG are further introduced, whose reflection spectrum is shown in Fig. 2(d).

We first investigate the resonant coupling behavior of a plane wave into the resonant mode supported by a single-layer Si MG. The metagrating, as shown in Fig. 2(a), is composed of amorphous Si with a refractive index of 3.47, immersed in the silicon dioxide background with a refractive index of 1.44. The grating period Λ_1 is 650 nm, with a duty cycle of 0.65. Infinite length in the y-direction and periodicity in the x-direction are set. Note that the Si MG duty cycle is finely tuned to balance the coupling with waveguide modes and fabrication process precision. A small duty cycle will weaken the coupling, while a large duty cycle will lead to an ultra-small grating gap that creates nanofabrication challenges. If the thickness of Si MG in the z-direction is assumed to be infinite, the metagrating could be regarded as a waveguide array, supporting a series of orthogonal eigenmodes propagating in the z-direction. The dispersion of these eigenmodes with normalized wavelength λ/Λ_1 and propagation constant β_n is shown in Fig. 2(b). The curves in Fig. 2(b) represent two orthogonal waveguide array modes propagating along the z-direction within the grating under normal incidence across the normalized wavelength range of 1.6–2.5. Since both modes are even modes, their subscripts are labeled β_0 and β_2. Odd modes (such as β_1) and other higher-order modes cannot propagate within this spectral range.

When the metagrating is truncated into finite thickness tg_1, β_0 and β_2 modes will be reflected at the interface of $z = 0$ and $z = tg_1$. Due to the abrupt change in the refractive index at the interface, they can couple with each other. To avoid confusion, we define the hybrid mode formed by the coupling between β_0 and β_2 as β'_n. In fact, new orthogonal modes without interaction while reflected at the interface, also called supermodes in Ref. 53, can be obtained by the diagonalization. When the coupled mode β'_n propagates in the metagrating, the accumulation phase φ_n is acquired. The metagrating actually acts like a Fabry–Pérot cavity. For a normal incident plane wave onto the Si MG (from bottom to top) [Fig. 2(a)], these new orthogonal modes are excited and go back and forth between two interfaces. When the accumulation phase in a round trip satisfies the Fabry–Pérot resonance condition $\varphi_n = 2n\pi$, where n is an integer, resonance happens and finally leads to an abrupt transition in the reflection spectrum in Fig. 2(d). Note that only the zeroth diffraction order of the Si MG exists under normal incidence, while higher-order diffraction modes (including the first) propagate as evanescent waves. Therefore, within the λ/Λ_1 range of 1.6–2.5, the transmission/reflection characteristics of the zeroth diffraction order arise from the mutual coupling and coherent superposition of the β_0 and β_2 modes.

For the combined grating-waveguide system [Fig. 2(c)], according to Eq. (1), the first diffraction order of the grating couples to the waveguide when wavevector matching ($\lambda/\Lambda_1 = n_{\text{eff}}$) is achieved. To couple the resonant mode into the waveguide mode, we further tune the resonant wavelength of Si MG to satisfy the wavevector matching condition in Eq. (1). The thickness t_1 of the topmost waveguide is 131 nm. The effective refractive index of the waveguide mode is 2.41, indicating that the matching wavelength is $\lambda/\Lambda_1 = 2.41$. We simulate the reflection spectrum of the system combined by Si MG and the waveguide, as shown in Fig. 2(e). The distance d_1 between the Si waveguide and the Si MG is 241 nm. Since Eq. (1) is independent of the thickness of Si MG, one can observe that sharp transition of reflection along a vertical line across all thickness in Fig. 2(e). What's more, by tailoring the thickness, the resonant mode of the individual Si MG will intersect with the vertical line, resulting in anti-crossing behavior in Fig. 2(e).[54] The anti-crossing behavior in Fig. 2(e) suggests the creation of a hybrid mode of the resonant metagrating mode β'_n and waveguide mode, equivalent to converting the zeroth diffraction into a waveguide-couplable first diffraction, which will help to boost the coupling efficiency. For demonstration, we present the field pattern at different wavelengths for the fixed thickness of $tg_1/\Lambda_1 = 1.31$. For wavelengths of 1.41 μm, which is far away from the anti-crossing region, the field pattern is mostly localized in the Si MG, as shown in Fig. 2(f). In contrast, for a wavelength of 1.55 μm, which is situated in the anti-cross region, the field pattern shows localization in both the Si MG and waveguide, as shown in Fig. 2(g). Due to mirror symmetry, the input plane wave will be coupled into two waveguide modes with wavevector components of k_x and $-k_x$.

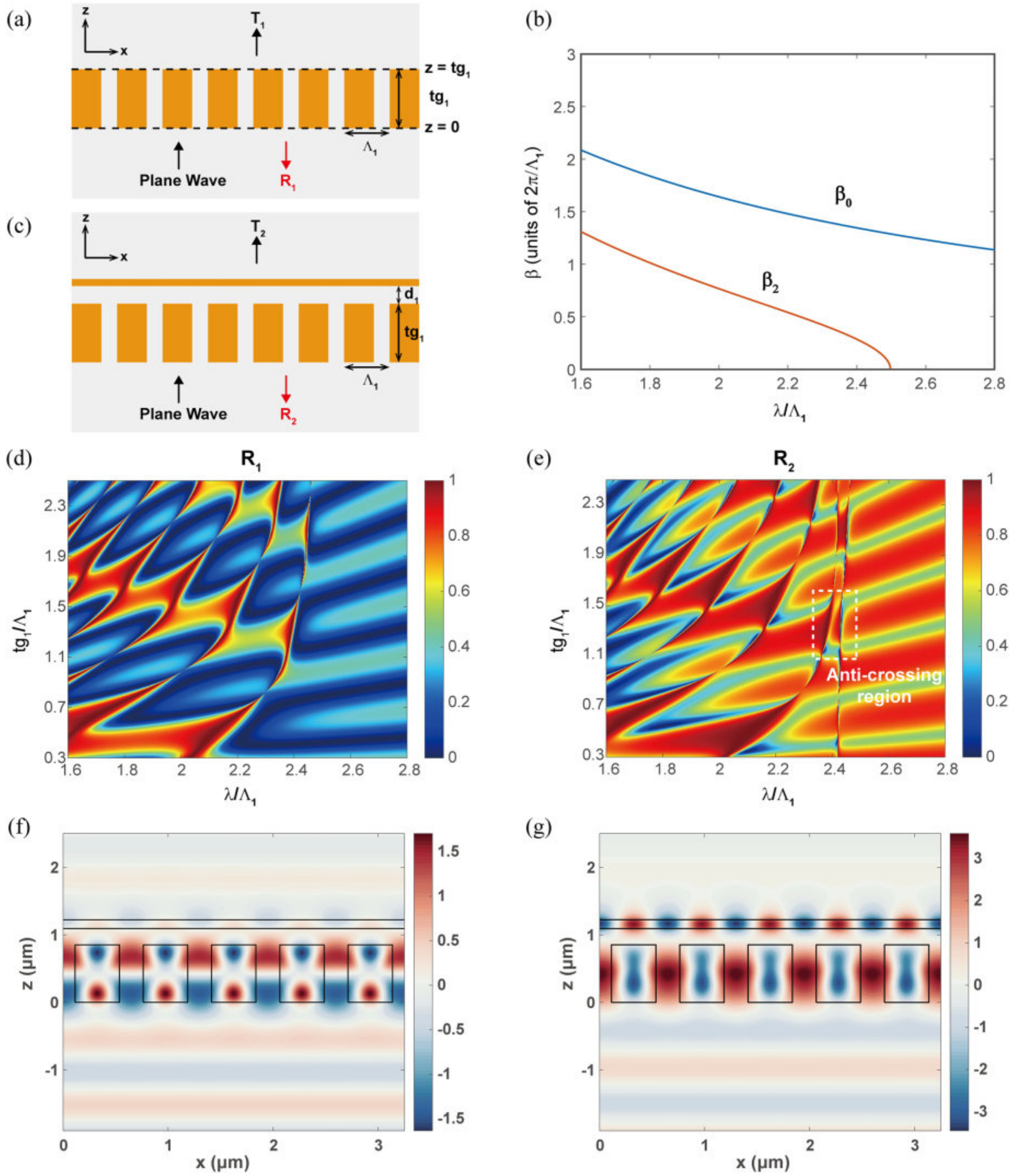

FIG. 2. Design and mode coupling mechanism analysis of Si MG and the waveguide structure. (a) Schematic cross-sectional view of Si MG in the xz-plane. The structure is assumed to be infinitely long in the y-direction and periodically repeated in the x-direction. A TE-polarized plane wave is incident from below. (b) The relationship between the propagation constant β in the z-direction and the normalized wavelength λ/Λ_1 for the waveguide array modes in the Si MG. (c) Schematic xz-plane cross-sectional view of the Si MG integrated with a waveguide. (d) Reflectance spectrum R1 of the Si MG under plane wave incidence. Both the grating thickness tg_1 and the wavelength λ are normalized by the grating period Λ_1. (e) Reflectance spectrum R2 of the combined Si MG and waveguide structure under plane wave incidence. (f) Optical field distribution far from the anti-crossing region. The black solid lines represent the contours of the grating and waveguide structure. (g) Optical field distribution at the center of the anti-crossing region.

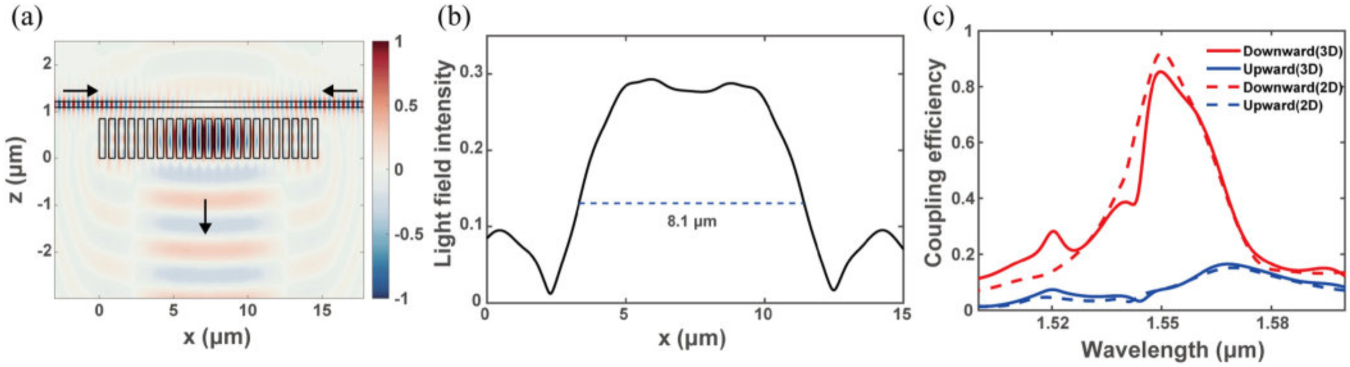

FIG. 3. Optical field distribution and coupling efficiency in waveguide-to-free-space coupling. (a) xz-plane optical field intensity distribution of light symmetrically incident from both ends of the waveguide and coupled out through the grating. Arrows indicate the directions of light input and output, with the structure's contour also shown. (b) Optical field intensity profile at $z = -1.5\,\mu$m. (c) Wavelength-dependent coupling efficiency of the light emitted upward and downward through the grating from the planar waveguide.

B. Uniform and efficient light coupling via Si MG design

The above analysis finally guides us to design the Si MG for high-efficient coupling and uniform intensity distribution. To verify the performance, we first conducted two-dimensional (2D) finite-difference time-domain (FDTD) simulations for the coupling process. The incident wavelength is set to $1.55\,\mu$m with TE polarization. As expected, two identical waveguide modes propagating in the waveguide are transformed into a vertically emitting beam in free space with a flat wavefront [Fig. 3(a)]. We further extracted the Ey intensity distribution at the $z = -1.5\,\mu$m plane, as illustrated in Fig. 3(b). Within the range $x = 5$–$10\,\mu$m, the intensity distribution exhibits a flat-top profile, with a large full width at half maximum (FWHM) of $8.1\,\mu$m. On the other hand, the upward and downward coupling efficiencies are plotted in Fig. 3(c) (dashed lines). At the central wavelength of $1.55\,\mu$m, the downward coupling efficiency reaches 90%, while the upward coupling efficiency is only 7%, implying high-efficiency performance. Furthermore, considering experimental feasibility, we also conduct three-dimensional (3D) FDTD simulations, in which the waveguide and Si MG both have a length of $3\,\mu$m in the y-direction. To suppress the higher-order waveguide modes, one can design a taper structure between a $0.5\,\mu$m-wide single-mode waveguide and a $3\,\mu$m-wide waveguide through adiabatic operation, ensuring single-mode transmission of incident light. As presented in solid lines in Fig. 3(c), a slightly lower efficiency of 84% in the downward channel can be observed. All of these results demonstrate the high-efficiency and uniform output beam from the upper Si MG.

C. Efficient light absorption via Ge MG design

Next, we consider how to efficiently absorb the output beam from the upper Si MG, by a lower Ge MG. The refractive index of Ge near $1.55\,\mu$m is 4.275. A thin Ge film with a thickness tg_2 of 466 nm is chosen. Then, to match the central wavelength of

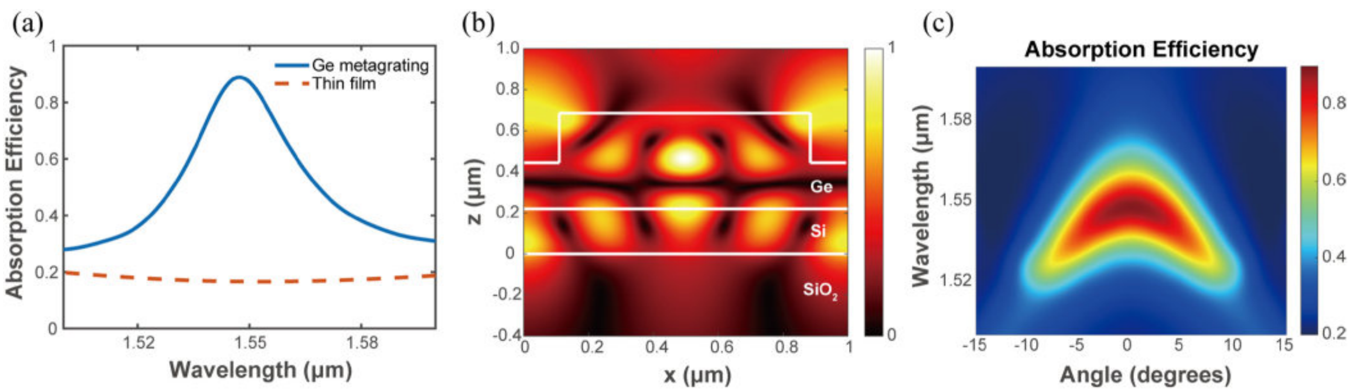

FIG. 4. Light absorption performance of Ge MG. (a) Absorption spectrum of the composite structure consisting of the Ge MG and the underlying Si slab waveguide under ideal plane wave incidence, with the absorption spectrum of a Ge thin film of the same thickness shown as a reference. (b) Electric field intensity distribution of the composite structure in the xz-plane, with solid white lines indicating the structural contours. (c) Absorption spectrum of the composite structure as a function of wavelength and incident angle.

1.55 μm and enhance the absorption, the Ge film is structured into a metagrating with a period Λ_2 of 993 nm, a duty cycle of 0.78, and an etch depth *te* of 242 nm. An additional 220 nm-thick Si slab waveguide is beneath the metagrating, which is a typical thickness in CMOS fabrication. Similar to the Si MG, the design of Ge MG aims to achieve high absorption efficiency via guided-mode resonance near the central wavelength of 1.55 μm, and, thus, we set the duty cycle to 0.78 to strike a trade-off between absorption efficiency and fabrication precision constraints. 3D FDTD simulations for the structure composed of the Ge MG and the Si slab waveguide are conducted. In the 3D simulations, the length and width of Ge MG are 15 and 5 μm, respectively. Figure 4(a) shows the simulated absorption spectrum of the metagrating (solid line), compared with the absorption spectrum of a Ge thin film with the same thickness (dashed line). Obviously, the Ge MG achieves a strong absorption peak of nearly 90% at the central wavelength of 1.55 μm, with a full width at half maximum (FWHM) of 30 nm. In contrast, the Ge thin film of the same thickness has an absorption efficiency of merely 16% at 1.55 μm. To understand the mechanism of the enhanced absorption, Fig. 4(b) presents the near-field xz-plane profile of the grating at 1.55 μm. It can be seen that light field is localized in the Ge MG structure and the intensity is enhanced by

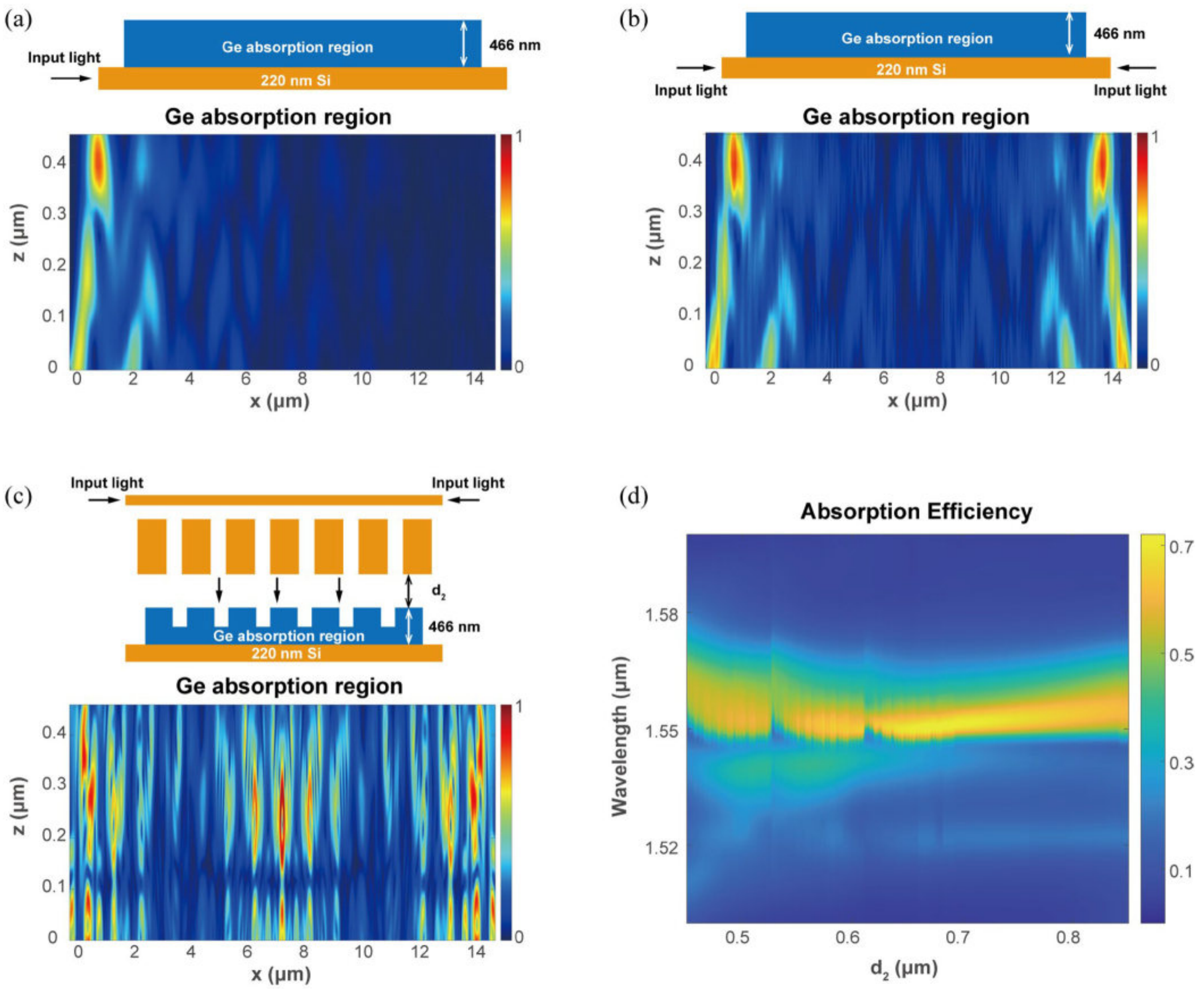

FIG. 5. Optical field distribution and absorption performance in Ge regions with waveguide-integrated bilayer metagratings. (a)–(c) Optical power distribution in the Ge absorption region (xz-plane) for different coupling schemes: (a) single-sided waveguide-coupled, (b) double-sided waveguide-coupled, and (c) bilayer metagrating coupled proposed in this work. (d) Relationship between the overall absorption efficiency of the bilayer metagrating and the grating interlayer spacing d_2 at different wavelengths.

the guided-mode resonance, leading to high absorption efficiency in Ge. Notably, the Ge MG designed using Ge on oxide can also achieve high absorption efficiency through analogous methods, thereby expanding the structural applicability. We also simulate the angle-dependent absorption of Ge MG in Fig. 4(c). It is evident that strong absorption is maintained within an incidence angle range of −5° to 5°.

D. Performance of waveguide-integrated bilayer metagratings and their impact on photodetector characteristics

Finally, we evaluate the overall performance of the waveguide-integrated bilayer metagratings, composed of the Si MG and the Ge MG designed above. We begin to discuss the light field uniformity in the Ge absorption region and the total absorption efficiency of waveguide-integrated bilayer metagratings. First, we compare the differences in the light field uniformity in the Ge absorption region between the waveguide-integrated bilayer metagratings coupling method and the conventional waveguide evanescent coupling method. Figure 5(c) presents the optical power intensity distribution (on the xz-plane) in the Ge absorption region under the waveguide-integrated bilayer metagrating coupling scheme, as simulated by 3D FDTD near the 1.55 μm wavelength. For comparison, Figs. 5(a) and 5(b) illustrate the schematic diagrams and corresponding optical power intensity distributions for the single-sided and double-sided waveguide coupling schemes in the Ge absorption region. In all three cases, the length, width, and thickness of

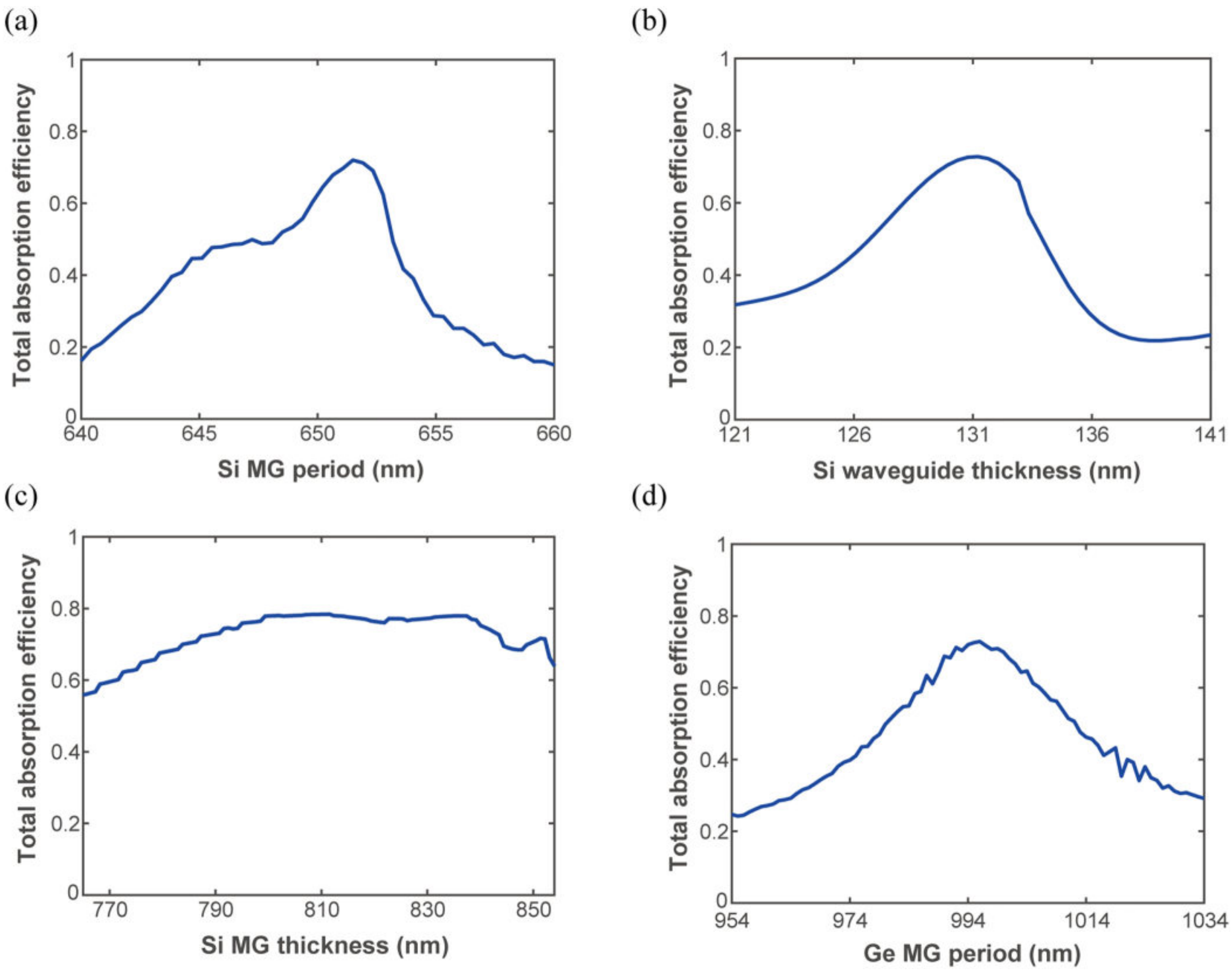

FIG. 6. Impact of structural parameter deviations on the total absorption efficiency of the waveguide-integrated bilayer metagratings. At the central wavelength of 1.55 μm, the total absorption efficiency of the structure under variations in (a) the Si MG period Λ_1, (b) Si waveguide thickness t_1, (c) Si MG thickness tg_1, and (d) Ge MG period Λ_2.

the Ge absorption region are identical, except that in Fig. 5(c), the Ge is etched into a grating structure.

It can be observed that, for single-sided waveguide coupling, the incident light is primarily concentrated at the front of the absorption region. Double-sided waveguide coupling shows some improvement by concentrating light on both sides, yet the central portion of the Ge absorption region still exhibits weak light intensity. In contrast, the incident light modulated by the metagrating achieves a more uniform intensity distribution across the entire absorption region. For photodetectors, non-uniform light absorption can lead to the accumulation of a large number of photogenerated electron–hole pairs in certain areas of the absorption region, causing pileup and counteracting the built-in electric field. This hinders the transport of carriers from the absorption layer to the external circuit. In such cases, the space-charge effect occurs, where the output photocurrent ceases to increase with increasing input optical power. Therefore, improving the uniformity of the optical field helps to mitigate the space-charge effect and increases the input optical power at which output current saturation occurs.[16,17]

The total absorption efficiency of the structure is influenced by the interlayer spacer thickness d_2 between the two gratings, and we have evaluated this effect. For the simulation results in Fig. 5(d), the absorption efficiency of the Ge MG at a wavelength of 1.55 μm achieves a maximum value exceeding 70%, indicating lower parametric sensitivity. In addition, we evaluate the impact of parameter deviations in the Si MG period Λ_1, Si MG thickness tg_1, Si waveguide thickness t_1, and Ge MG period Λ_2 on the total absorption efficiency of the structure at the central wavelength of 1.55 μm, as shown in Fig. 6. The results demonstrate that the performance is insensitive to tg_1 but relatively higher sensitive to Λ_1, t_1, and Λ_2. We also present the temperature-dependent total absorption efficiency of our proposed structure at the central wavelength of 1.55 μm, as shown in Fig. 7. The total absorption efficiency reaches a maximum of 72% near 28 °C, with only a 10% efficiency reduction even under ±20 °C temperature variations. Over 50% absorption efficiency is retained at temperatures from 0 to 60 °C. The results indicate that the performance does not degrade significantly under temperature variations.

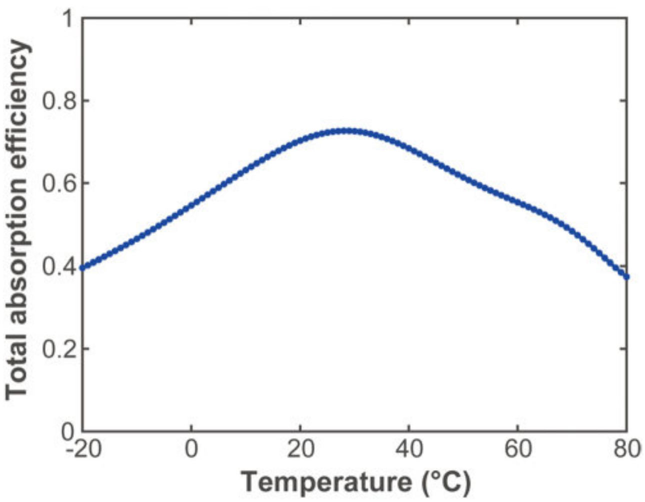

FIG. 7. Total absorption efficiency at the central wavelength vs temperature.

Furthermore, the design of the Ge MG enhances the absorption of incident light, thereby contributing to the improvement of the responsivity of photodetectors. Under ideal conditions, a single photon can generate one electron–hole pair, corresponding to 100% quantum efficiency. Under this condition, the relationship between responsivity R and wavelength λ can be expressed as follows:

$$R = R_{\max} \times Ae = \frac{q}{\hbar\omega} \times Ae \approx \frac{\lambda(\mu\text{m})}{1.24} \times Ae. \tag{2}$$

Here, q represents the electron charge, $\hbar$ is the reduced Planck constant, and Ae is the absorption efficiency of the overall structure. Consequently, the maximum responsivity R of the entire structure can reach 0.9 A/W. For a more common case in photonic integrated circuits, the proposed structure can also be configured for single-sided incidence. The maximum responsivity decreases to 0.74 A/W but exhibits no significant impact on the light field uniformity within the Ge absorption region.

In addition, Ge MG has the potential to maintain a high 3 dB opto-electrical (OE) bandwidth since we enhance the absorption efficiency while reducing its thickness to only 466 nm. The theoretical 3 dB OE bandwidth of conventional p–i–n photodetectors is primarily determined by the transit time-limited bandwidth (f_{TR}) and the resistance–capacitance (RC) bandwidth (f_{RC}). f_{TR} and f_{RC} can be approximately calculated using the following equations:[19,44]

$$f_{\text{TR}} \approx 0.45 \frac{v_{\text{sat}}}{d_i}, \tag{3}$$

$$f_{\text{RC}} = \frac{1}{2\pi C(R_{\text{Load}} + R_S)}, \tag{4}$$

$$f_{3\text{ dB}} = \frac{1}{\sqrt{f_{\text{RC}}^{-2} + f_{\text{TR}}^{-2}}}. \tag{5}$$

In this case, as an approximation, we regard the Ge MG as a uniform thin-film structure with a thickness of 466 nm and a length of 15 μm. Figure 8 presents the cross-sectional view of the proposed p–i–n structure in the yz-plane, illustrating the positions of the metal electrodes (including the anode and cathode). Such a configuration of the p-contact metal can avoid the light-blocking

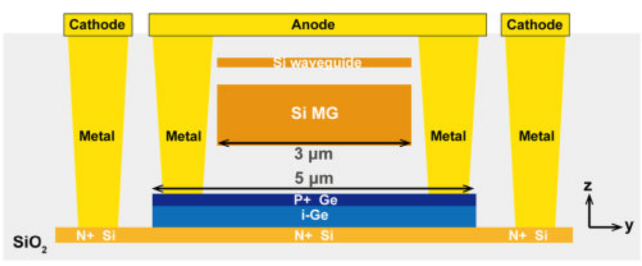

FIG. 8. Schematic diagram of the geometric configuration of the p–i–n structure.

issue when the light enters the Ge layer. Therefore, we stated that both the top Si waveguide and the Si MG have a width of 3 μm along the y-direction, whereas the Ge MG has a y-directional width of 5 μm. This additional width is reserved for fabricating metal electrodes at the top of Ge. Additionally, the top region of Ge MG is P^+-doped, while the underlying Si slab waveguide beneath Ge MG is N^+-doped. d_i represents the intrinsic layer thickness (assumed to be 366 nm, for 100 nm P^+-doped Ge layer forming the p–i–n junction), v_{sat} is the saturation hole velocity (6×10^6 cm/s), C is the device capacitance (3.32×10^{-14} F), R_{Load} is the load resistance (50 Ω), and R_S is the series resistance (assumed to be 0). Therefore, f_{TR} is approximately 74 GHz and f_{RC} is 96 GHz. The theoretical 3 dB OE bandwidth of the photodetector is approximately 58 GHz. Actually, the size of the Ge region can be customized to achieve the desired bandwidth, and the grating dimensions can be adjusted accordingly to maintain a uniform light field distribution.

III. CONCLUSION

In summary, we demonstrate a waveguide-integrated bilayer metagratings framework that mitigates the uniformity-efficiency trade-off in waveguide-coupled photodetectors by decoupling light redistribution from absorption processes. The Si MG couples out the waveguide mode and redistributes its intensity uniformly via resonant mode coupling between the waveguide and the metagrating, achieving a coupling efficiency as high as 84%. The Ge MG achieves 90% absorption efficiency through GMR, which is five times higher than that of a conventional thin film with the same thickness. This dual-functional architecture maintains over 70% system-level absorption efficiency while ensuring light field uniformity in the Ge region, demonstrating the potential to transcend the limitations of evanescent coupling methods. We investigate the parameter sensitivity and the impact of temperature variations on the total absorption efficiency. By providing independent control over light redistribution and absorption enhancement, our approach paves the way for photodetectors capable of simultaneously achieving high saturation power and responsivity. The decoupling principle offers a scalable strategy for III–V/Si hybrid integration in applications such as LIDAR receivers and programmable quantum photonic circuits.

ACKNOWLEDGMENTS

This work was supported by the National Natural Science Foundation of China (NSFC) under Grant No. 62035016 and the Guangdong Basic and Applied Basic Research Foundation under Grant No. 2023B1515040023.

AUTHOR DECLARATIONS

Conflict of Interest

The authors have no conflicts to disclose.

Author Contributions

Xin Zhou: Conceptualization (lead); Data curation (equal); Methodology (lead); Software (equal); Validation (equal); Writing – original draft (equal); Writing – review & editing (equal). **Zepeng Zhuang:** Data curation (equal); Software (equal); Validation (equal); Writing – original draft (equal); Writing – review & editing (equal). **Xintao He:** Supervision (equal); Writing – original draft (equal); Writing – review & editing (equal). **Jianwen Dong:** Conceptualization (equal); Data curation (equal); Funding acquisition (lead); Supervision (equal); Writing – original draft (equal); Writing – review & editing (equal).

DATA AVAILABILITY

The data that support the findings of this study are available from the corresponding author upon reasonable request.

REFERENCES

[1] D. Thomson, A. Zilkie, J. E. Bowers, T. Komljenovic, G. T. Reed, L. Vivien, D. Marris-Morini, E. Cassan, L. Virot, J.-M. Fédéli, J.-M. Hartmann, J. H. Schmid, D.-X. Xu, F. Boeuf, P. O'Brien, G. Z. Mashanovich, and M. Nedeljkovic, J. Opt. **18**, 073003 (2016).
[2] S. Shekhar, W. Bogaerts, L. Chrostowski, J. E. Bowers, M. Hochberg, R. Soref, and B. J. Shastri, Nat. Commun. **15**, 751 (2024).
[3] M. Asghari and A. V. Krishnamoorthy, Nat. Photonics **5**, 268 (2011).
[4] K. Yamada, T. Tsuchizawa, H. Nishi, R. Kou, T. Hiraki, K. Takeda, H. Fukuda, Y. Ishikawa, K. Wada, and T. Yamamoto, Sci. Technol. Adv. Mater. **15**, 024603 (2014).
[5] L. Vivien and L. Pavesi, *Handbook of Silicon Photonics* (CRC Press, 2013).
[6] D. Marpaung, J. Yao, and J. Capmany, Nat. Photonics **13**, 80 (2019).
[7] C. H. Cox, E. I. Ackerman, G. E. Betts, and J. L. Prince, IEEE Trans. Microwave Theory Tech. **54**, 906 (2006).
[8] H. T. Chen, P. Verheyen, P. De Heyn, G. Lepage, J. De Coster, P. Absil, G. Roelkens, and J. Van Campenhout, J. Lightwave Technol. **33**, 820 (2015).
[9] Y. Li, Y. Zhang, L. Zhang, and A. W. Poon, Photonics Res. **3**, B10 (2015).
[10] T.-C. Tzu, K. Sun, R. Costanzo, D. Ayoub, S. M. Bowers, and A. Beling, IEEE J. Sel. Top. Quantum Electron. **25**, 1 (2019).
[11] L. Vivien, A. Polzer, D. Marris-Morini, J. Osmond, J. M. Hartmann, P. Crozat, E. Cassan, C. Kopp, H. Zimmermann, and J. M. Fédéli, Opt. Express **20**, 1096 (2012).
[12] J. Song, S. Yuan, C. Cui, Y. Wang, Z. Li, A. X. Wang, C. Zeng, and J. Xia, Nanophotonics **10**, 1081 (2021).
[13] J. Michel, J. Liu, and L. C. Kimerling, Nat. Photonics **4**, 527 (2010).
[14] C.-H. Lin, D.-W. Huang, T.-T. Shih, H.-C. Kuo, and S.-W. Chang, Opt. Express **29**, 10364 (2021).
[15] X. Li, Y. Liu, R. Song, C. Li, S. Wang, W. Yue, Z. Tu, X. Chen, Y. Cai, W. Wang, and M. Yu, Opt. Express **31**, 3325 (2023).
[16] K. J. Williams, R. D. Esman, and M. Dagenais, IEEE Photonics Technol. Lett. **6**, 639 (1994).
[17] A. Ramaswamy, M. Piels, N. Nunoya, T. Yin, and J. E. Bowers, IEEE Trans. Microwave Theory Tech. **58**, 3336 (2010).
[18] M. J. Byrd, E. Timurdogan, Z. Su, C. V. Poulton, N. M. Fahrenkopf, G. Leake, D. D. Coolbaugh, and M. R. Watts, Opt. Lett. **42**, 851 (2017).
[19] X. Hu, D. Wu, H. Zhang, W. Li, D. Chen, L. Wang, X. Xiao, and S. Yu, Photonics Res. **9**, 749 (2021).
[20] H. Cao, Y. Xiang, W. Sun, J. Xie, J. Guo, Z. Yu, L. Liu, Y. Shi, and D. Dai, ACS Photonics **11**, 1761 (2024).
[21] G. Chen, Y. Yu, X. Xiao, and X. Zhang, Opt. Express **24**, 10030 (2016).
[22] Y. Zuo, Y. Yu, Y. Zhang, D. Zhou, and X. Zhang, Opt. Lett. **44**, 3338 (2019).
[23] X. Hu, D. Wu, H. Zhang, W. Li, D. Chen, L. Wang, X. Xiao, and S. Yu, Opt. Express **28**, 38343 (2020).
[24] Y. Ra'di, D. L. Sounas, and A. Alù, Phys. Rev. Lett. **119**, 067404 (2017).
[25] W. Shi, W. Deng, W. Liu, Z. Zhuang, Z. Fan, and J. Dong, Chin. Opt. Lett. **18**, 073601 (2020).

[26]D. Sell, J. Yang, S. Doshay, R. Yang, and J. A. Fan, Nano Lett. **17**, 3752 (2017).
[27]Y. Meng, Y. Chen, L. Lu, Y. Ding, A. Cusano, J. A. Fan, Q. Hu, K. Wang, Z. Xie, Z. Liu, Y. Yang, Q. Liu, M. Gong, Q. Xiao, S. Sun, M. Zhang, X. Yuan, and X. Ni, Light: Sci. Appl. **10**, 235 (2021).
[28]J. Y. Rhee, Y. J. Yoo, K. W. Kim, Y. J. Kim, and Y. P. Lee, J. Electromagn. Waves Appl. **28**, 1541 (2014).
[29]S. Kim, D. A. Westly, B. J. Roxworthy, Q. Li, A. Yulaev, K. Srinivasan, and V. A. Aksyuk, Light: Sci. Appl. **7**, 72 (2018).
[30]C. Ropp, A. Yulaev, D. Westly, G. Simelgor, and V. Aksyuk, Opt. Express **29**, 14789 (2021).
[31]L. Zhu, W. Yang, and C. Chang-Hasnain, Opt. Express **25**, 18462 (2017).
[32]X. Guo, Y. Ding, X. Chen, Y. Duan, and X. Ni, Sci. Adv. **6**, eabb4142 (2020).
[33]X. Chen, C. Li, C. K. Y. Fung, S. M. G. Lo, and H. K. Tsang, IEEE Photonics Technol. Lett. **22**, 1156 (2010).
[34]J. Yoon, J.-Y. Kim, J. Kim, H. Yoon, B. Neşeli, H.-H. Park, and H. Kurt, Photonics Res. **11** (2023), 897.
[35]Z. Zhao and S. Fan, J. Lightwave Technol. **38**, 4435 (2020).
[36]R. Guo, S. Zhang, H. Gao, G. Senthil Murugan, T. Liu, and Z. Cheng, Photonics Res. **11**, 189 (2023).
[37]M. Kohli, D. Chelladurai, B. Vukovic, D. Moor, D. Bisang, K. Keller, A. Messner, T. Buriakova, M. Zervas, Y. Fedoryshyn, U. Koch, and J. Leuthold, ACS Photonics **10**, 3366 (2023).
[38]I. Khaw, B. Croop, J. Tang, A. Möhl, U. Fuchs, and K. Y. Han, Opt. Express **26**, 15276 (2018).
[39]Y. Zhu, J. Wang, W. Xie, B. Tian, Y. Li, E. Brainis, Y. Jiao, and D. Van Thourhout, Opt. Express **25**, 33297 (2017).
[40]L. Tang, D. A. Miller, A. K. Okyay, J. A. Matteo, Y. Yuen, K. C. Saraswat, and L. Hesselink, Opt. Lett. **31**, 1519 (2006).
[41]Y. Cui, Y. He, Y. Jin, F. Ding, L. Yang, Y. Ye, S. Zhong, Y. Lin, and S. He, Laser Photonics Rev. **8**, 495 (2014).
[42]X.-L. Hu, F. Li, S.-H. Xu, and W.-J. Liu, Opt. Lett. **48**, 4033 (2023).
[43]M. R. Lien, N. Wang, J. Wu, A. Soibel, S. D. Gunapala, H. Wang, and M. L. Povinelli, Nano Lett. **22**, 8704 (2022).
[44]Z. Liu, J. Liu, B. Cheng, J. Zheng, C. Li, C. Xue, and Q. Wang, J. Appl. Phys. **124**, 053101 (2018).
[45]Z. Chen, Y. Weng, J. Liu, N. Guo, Y. Yu, and L. Xiao, Photonics Res. **9**, 27 (2020).
[46]D. Wei, A. A. Dadey, J. A. McArthur, S. R. Bank, and J. C. Campbell, ACS Photonics **11**, 484 (2024).
[47]K. Y. Lee, K. W. Yoo, S. Cheon, W.-J. Joo, J. W. Yoon, and S. H. Song, Phys. Rev. Lett. **128**, 053002 (2022).
[48]Z.-P. Zhuang, H.-L. Zeng, X.-D. Chen, X.-T. He, and J.-W. Dong, Phys. Rev. Lett. **132**, 113801 (2024).
[49]W.-N. Liu, R. Chen, W.-Y. Shi, K.-B. Zeng, F.-L. Zhao, and J.-W. Dong, Nanophotonics **9**, 3443 (2020).
[50]Y. Zhou, R. Zou, J. Zhan, Y. Wang, D. Dai, P. K. Choudhury, A. Forbes, and Y. Ma, Laser Photonics Rev. **19**, 2401391 (2024).
[51]W. Yang, J. Zhou, D. P. Tsai, and S. Xiao, Photonics Insights **3**, R04 (2024).
[52]W. D. Sacher, Y. Huang, L. Ding, B. J. F. Taylor, H. Jayatilleka, G.-Q. Lo, and J. K. S. Poon, Opt. Express **22**, 10938 (2014).
[53]V. Karagodsky and C. J. Chang-Hasnain, Opt. Express **20**, 10888 (2012).
[54]V. Karagodsky, F. G. Sedgwick, and C. J. Chang-Hasnain, Opt. Express **18**, 16973 (2010).